ACS Catalysis

Research Article

pubs.acs.org/acscatalysis

Stability of Dealloyed Porous Pt/Ni Nanoparticles

Claudio Baldizzone,[*,†] Lin Gan,[‡] Nejc Hodnik,[†,#] Gareth P. Keeley,[†] Aleksander Kostka,[§] Marc Heggen,[∥] Peter Strasser,[⊥] and Karl J. J. Mayrhofer[†]

[†]Department of Interface Chemistry and Surface Engineering Max-Planck-Institut für Eisenforschung GmbH, Max-Planck-Strasse 1, 40237 Düsseldorf, Germany

[‡]Division of Energy & Environment, Graduate School at Shenzhen, Tsinghua University, 518055 Shenzhen, P.R. China

[§]Department of High Temperature Materials, Max-Planck-Institut für Eisenforschung GmbH, Max-Planck-Strasse 1, 40237 Düsseldorf, Germany

[∥]Ernst Ruska Center for Microscopy and Spectroscopy with Electrons, Forschungzentrum Jülich GmbH, 52425 Jülich, Germany

[⊥]Electrochemical Energy, Catalysis and Materials Science Laboratory, Department of Chemistry, Chemical Engineering Division, Technical University Berlin, 10623 Berlin, Germany

Supporting Information

ABSTRACT: We provide a comprehensive durability assessment dedicated to a promising class of electrocatalysts for the oxygen reduction reaction (i.e., porous platinum nanoparticles). The stability of these nanoengineered open structures is tested under two accelerated degradation test conditions (ADT), particularly selected to mimic the potential regimes experienced by the catalyst during the operative life of a fuel cell (i.e., load cycles (up to 1.0 V_{RHE}) and start-up cycles (up to 1.4 V_{RHE})). To understand the evolution of the electrochemical performance, the catalyst properties are investigated by means of fundamental rotating disc electrode studies, identical location-transmission electron microscopy (IL-TEM) coupled with electron energy loss spectroscopy chemical mapping (IL-EELS), and post-use chemical analysis and online highly sensitive potential resolved dissolution concentration monitoring by scanning flow cell inductively coupled plasma-mass spectrometry (SFC-ICP-MS). The experimental results on the nanoporous Pt revealed distinctive degradation mechanisms that could potentially affect a wide range of other nanoengineered open structures. The study concludes that, although providing promising activity performance, under the relevant operational conditions of fuel cells, the nanoporosity is only metastable and subjected to a progressive reorganization toward the minimization of the nanoscale curvature. The rate and pathways of this specific degradation mechanism together with other well-known degradation mechanisms like carbon corrosion and platinum dissolution are strongly dependent on the selected upper limit potential, leading to distinctly different durability performance.

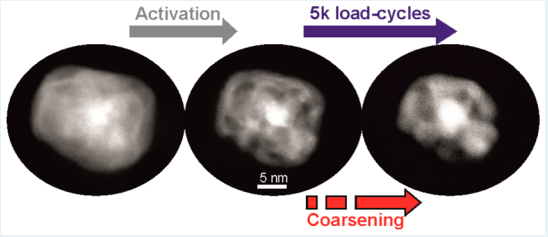

KEYWORDS: *porous metals, ORR, fuel cells, platinum alloys, stability*

INTRODUCTION

Meeting the increasing energy demands of the growing global economy requires the development of dependable and sustainable energy sources, as well as conversion and storage technologies. In this context, proton exchange membrane fuel cells are likely to play an important role due to their relatively high energy conversion efficiency and to their zero CO_2 emission. Nonetheless, to be considered as a competitive alternative to the state of the art internal combustion engines, certain crucial issues need to be resolved. Above all, drastically reducing the high platinum loadings (required to drive the sluggish oxygen reduction reaction, ORR) is an imperative condition for lowering the costs of these devices.[1] Among the several solutions proposed by the scientific literature, one interesting class of functional materials with enhanced performance is the so-called nanoporous metals.[2,3] Because of their unique interconnected and open percolated structure, porous metals have attracted a lot of attention in the field of catalysis and electrocatalysis. For fuel cell applications, nanoporous platinum is produced via a wide range of techniques (e.g., templating and colloidal methods,[4−6] electrodeposition, and other self-organization routes).[7−10] Additionally, a widely common approach for the formation of these structures consists of exploiting a well-known corrosion mechanism, namely, (electro-)chemical dealloying.[2] In this way, the porous material is obtained by selectively leaching the less noble element from a binary alloy leaving behind the desired percolated structure. Besides Pt porous films, this approach can also be readily applied to other nanostructures more suitable for implementation in the catalyst layer of a fuel cell electrode, namely, nanoparticles or nanowires.[11−20] However, to nanoengineer porosity at a particle level, the selection of a

Received: June 3, 2015
Revised: July 9, 2015
Published: July 30, 2015

DOI: 10.1021/acscatal.5b01151
ACS Catal. 2015, 5, 5000−5007

defined size distribution is pivotal. Indeed, although for bulk films the critical potential leading to porosity formation is predominantly dependent on the composition of the alloy,[21,22] for a nanoparticulate system, its value additionally depends on the size of the single nanoparticle.[18,23,24] Small-sized particles tend to form a core−shell and/or multicoreshell structure upon dealloying, whereas for larger sizes, an increasing fraction of nanoparticles yields a complex porous network. The reason for such morphological dichotomy lies in a kinetic effect, for which the critical potential associated with porosity formation increases as $1/r$ (where r is the particle radius).[25] Experimentally, such behavior has been confirmed for several binary systems (e.g., Cu/Pt, Co/Pt, Ag/Au) and for the specific case of Ni/Pt, where the lower limit size for the formation of fully porous particles was found equal to around 15 nm.[18,23,26−28] The enhanced activity of such nanoporous systems for the ORR in fuel cells has been ascribed to a combination of several effects: (i) the increased surface area to volume ratio;[8,29] (ii) the ligand and strain effect related to the presence of residual subsurface alloy element in the ligaments;[30] (iii) a confinement effect within the nanoporous structure that leads to increased residence time at the active surface[16,18,31−35] or to proximity effects;[36−38] and lastly (iv), one other interesting aspect of the porous configuration is the intrinsic presence of a strong negative surface curvature (i.e., concave surfaces) coupled with a smaller fraction of low-coordinated atoms, which have been both proven to be favorable toward ORR.[10,39,40] Although porous nanoparticles may help increase the ORR efficiency in the early life stages, their usefulness is only assured as long as they can sustain their activity under the relevant operative conditions of fuel cells. As this delicate issue is typically less addressed in literature, we provide here a detailed durability assessment of a representative Pt nanoporous particulate system. Because the presence of a nonporous fraction could potentially hinder a reliable interpretation of the specific durability, we avoid employing a polydispersed catalyst. Instead, the material selected for the investigation consists of monodispersed $PtNi_3$ nanoparticles with a diameter of around 25 nm (for details concerning the synthesis and exact particle size distribution please refer to Figure S1 in the Supporting Information); the relatively narrow particle size distribution, the large diameter, and the composition are specifically selected to ensure that all the nanoparticles included in the samples reach a fully porous configuration with a 3:1 Pt:Ni ratio. Nickel was chosen as a representative alloying element, due to some of the most influential ORR activity enhancement studies and due to the widespread use of this element for the synthesis of a variety of open nanostructures.[14,20,35,40−49] To simulate the conditions associated with an operating fuel cell, the work includes two different accelerated degradation tests (ADTs) mimicking two common voltage regimes for cathode electrocatalysts, namely, "load cycles" (up to 1.0 V_{RHE}) and "start-up cycles" (up to 1.4 V_{RHE}).

RESULTS AND DISCUSSION

In general, dealloying can be triggered under the appropriate conditions either chemically by acid leaching or electrochemically by adjusting the potential of an immobilized catalyst.[8,9,50,51] Following the work of Erlebacher et al.,[13,18,52] the most suitable activation protocol selected for our investigation consists of 200 cycles between 0.05 and 1.2 V_{RHE} with a scan rate of 0.5 V s^{-1}. Figure 1 reports the evolution of the active surface area (ECSA), the Ni molar ratio during the activation procedure (A), and the intrinsic activity by means of Tafel plots compared to a standard Pt/C catalyst (B). With activation, the ECSA shows a rapid increase in the first 50 cycles, and it reaches a stable plateau after around 100 cycles. This active surface area enhancement is related to the formation of a porous structure coupled with dealloying triggered by the repeated oscillation between reductive and oxidative potentials. Indeed, parallel to the evolution in ECSA, also the Ni content in the catalyst assessed by post-mortem ICP-MS analysis appears to change drastically, dropping from the initial 75% to around 26% molar ratio. Thus, indicating an evolution from the initial 1:3 Pt:Ni ratio to a configuration closer to 3:1, a result completely consistent with other works concerning nano-engineered nanostructures.[18,41,48]

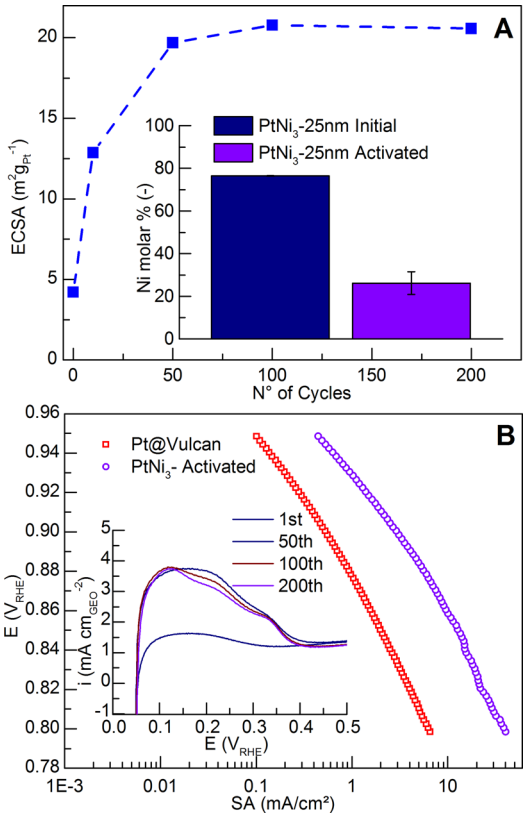

Figure 1. (A) Active surface area increase during activation as measured by CO-stripping and dealloying monitored by post-mortem ICP-MS analysis (inset). (B) Specific activity comparison by means of Tafel plot versus a standard Pt/C catalyst and evolution of the H_{upd} region with cycling (inset). The activity values were acquired in $HClO_4$ at room temperature with scan rate of 0.05 V s^{-1}.

The development of the percolated network related to the copious Ni dissolution (Figure S3) starts from the low coordinated surface sites and later continues to the core of the nanoparticles, as previously suggested.[18] Following the pore formation, the remnant activation cycles proceed to smoothen the newly formed and rough Pt-rich surface of the network ligaments, as supported by the evolution of the H_{upd} region features (Figure 1B, inset). Once activated, the catalyst shows a clear enhancement in specific activity (SA) and a shift in the onset potential for ORR (Figure S2) compared to state-of-the-art Pt/C catalysts, which can be attributed to the presence of remaining subsurface Ni, to eventual nanoconfinement, and/or to proximity effects. The specific activity taken at 0.9 V_{RHE} (2.6

DOI: 10.1021/acscatal.5b01151
ACS Catal. 2015, 5, 5000−5007

± 0.1 mA cm^{-2}) and the correlated Ni content are comparable to the values found by other groups,[18,47] proving our catalyst as an accurate representative of a general porous nanoparticle system. Although the mass activity (MA), being the product of SA and ECSA, increases significantly compared to the initial state, it is slightly lower than reported for other systems. Such discrepancy may be imputed to the larger particle size leading, in turn, to a generally smaller ECSA. To further investigate the process of activation, our analysis proceeded with the direct observation of the catalyst by means of scanning transmission electron microscopy (STEM) before and after the activation protocol. Figures 2 and S4 display HAADF-STEM micrographs

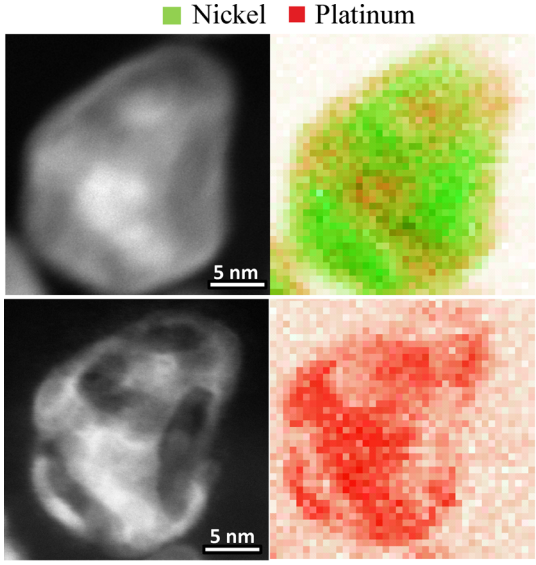

	Ni molar %	Pt molar %
Before	72	28
After	22	78

Figure 2. HAADF micrographs (left column) and EELS spectrum images (right column) of a single, representative nanoparticle before (upper row) and after (bottom row) activation (i.e., 200 cycles between 0.05 and 1.2 V_{RHE} at 0.5 V s^{-1}). Quantitative results of the overall compositional analysis on the nanoparticle (bottom table).

and EELS element concentration maps of the same particles obtained by means of identical location microscopy (for further details about the IL-approach please refer to the SI and previous works[53−55]). Confirming the observations from the electrochemical characterization, the nanoparticles nicely show the formation of a fully developed 3D network and a parallel strong depletion of the less noble element (i.e., Ni). The IL-EELS scans in Figure 2 display how, starting from a Ni-rich configuration, the nanoparticles evolve to a complex Platinum 3D structure containing pores with a diameter in the order of few nanometers. Moreover, while before activation brighter and darker patches in the HAADF micrographs could be attributed to fluctuations in Ni/Pt ratio, after activation the darker areas appear depleted of both elements, indicating the presence of a percolation network.[56] Also, by overlapping the before and after scans, it becomes obvious how the areas with an enhanced Ni signal match the locations of the pores, while the initial Pt-rich areas remain as ligaments afterward.

The porosity initiates where the Ni is relatively abundant and can proceed to the core of the nanoparticle when Pt is not sufficiently available to form a protective layer. Note that the dealloying process and its extent will largely depend on the particle composition and thus on synthesis conditions. In this particular case, compositional inhomogeneity partially arises from an element-specific anisotropic growth during the synthesis process. Namely, a large fraction of the as-received nanoparticles (Figure 2 and S4) display a near-spherical configuration coupled with a noticeable degree of faceting. Hence, considering the recent work of Gan et al.[57] on the synthesis of shape-controlled octahedral PtNi nanoparticles, the local Pt/Ni compositional fluctuations might be explained by a similar anisotropic Pt growth, where initially the nanoparticles evolve in a branched Pt-rich structure, on whose concave surfaces the Ni would preferentially deposit.

Having established the activated state of the catalyst and the initial electrochemical performance, the focus will be placed on the durability of the porous structures. To first investigate the stability under the nominal operative conditions expected in a fuel cell, an ADT of 10 800 cycles between 0.4 and 1.0 V_{RHE} at 1.0 V s^{-1} is applied. First, the active surface area monitored by means of CO-stripping steadily decreases throughout the whole degradation protocol, yielding a final loss of around 20% relative to the maximum value after activation (Figure 3A). To corroborate this observation, the evolution of the CVs at different stages of degradation is also followed (inset of Figure 3). Interestingly, the H_{upd} region of these CVs shows two important changes, namely, a slight dip in intensity and a

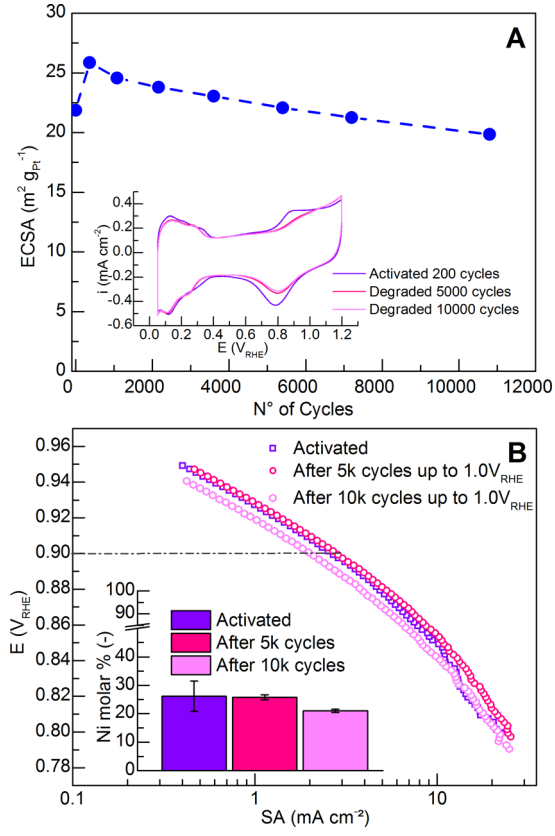

Figure 3. (A) ECSA vs degradation cycles, performed between 0.4 and 1.0 V_{RHE} at room temperature with 1.0 V s^{-1} scan rate, and representative CVs at defined intervals of the durability test (inset). (B) Tafel plots and Ni molar ratio evolution (inset) of the catalyst under study at the beginning of degradation, after 5000 and 10 000 cycles; the kinetic data are obtained by normalizing the currents by the active surface area measured after each degradation interval.

DOI: 10.1021/acscatal.5b01151
ACS Catal. 2015, 5, 5000−5007

reorganization of the peaks; although the former is connected to the above-mentioned loss in surface area, the latter can be attributed to the exposure of different crystal facets after the electrochemical treatment. Notably, a similar faceting was already reported in a previous work on the stability of Pt porous nanoparticles for high temperature applications.[26,45] The evolution of the intrinsic activity after 5000 and 10 000 cycles is shown in Figure 3B. The SA remains approximately constant for the first 5000 cycles, and only declines after another 5000 cycles by less than 20%. This decrease could be induced by the small decrease in Ni content observed by means of post-use ICP-MS analysis at the end of the degradation protocol, which corresponds to a gradual weakening of the ligand and geometric effect related to the presence of the alloying element in the pores' ligaments. To better understand the underlying process at the nanoscale, the study includes a further IL-HAADF-STEM investigation before and after 5000 "load cycles". Interestingly, the detailed observation of several locations pointed out a quite different degradation process compared to standard Pt and Pt alloy catalysts.[42,43,58−60] Under these potential conditions, Ostwald ripening and particle agglomeration are typically considered as the two main contributors to the loss of surface area. Here, instead, none of the above-mentioned mechanisms appears to play a significant role owing to the rather large particles and the upper limit potential applied. While the large interparticle distance substantially decreases the chance of coalescence,[61] cycling only up to 1.0 V_{RHE}, below the onset potential for significant Pt dissolution, does not trigger particle ripening by dissolution/redeposition.[62,63]

Instead, the reason for the decrease in active surface area can be related to a deterioration of the porous structure (Figure 4 and S5) by reorganization of the percolated network through surface atom mobility, driven by the minimization of the nanoscale curvature. As shown in Figure 4B, already after 5000 cycles, the outer ligaments of the nanoparticles appear to have vanished, leaving behind a more accessible but less complex structure. Besides producing a loss in active surface area, this relaxation of the porosity could also contribute to the decrease in specific activity, as it is necessarily coupled with a weakening of nanoconfinement/proximity effects. Moreover, the surface mobility of Pt atoms can lead to additional leaching of Ni atoms from the interior. Such findings are consistent with other works available in literature, as, for instance, reported by Wang et al.[14] and also anticipated by means of kinetic Monte Carlo simulations by the group of Erlebacher.[64] The progressive porosity coarsening of a nanoporous gold leaf (NPGL) has also been reported under prolonged exposure to concentrated nitric acid and was ascribed to the high surface diffusivity of gold atoms.[44]

Similarly, He et al. reported the observation of a potential induced coarsening of platinum nanocrystals by means of in situ electrochemical STM.[65,66] This phenomenon was confirmed also for PtCo surfaces and related to the fast surface diffusion of Pt adatoms in the double layer region.[67] Furthermore, also other works[68,69] on the surface diffusion processes at the electrode/electrolyte interfaces clearly indicate the influence of potential on the mobility of metal adatoms. Although a unanimous consensus on which potential range corresponds to the largest diffusion coefficient is yet to be achieved, it is reasonable to expect that a similar process could take place in our system, leading to the progressive migration of platinum atoms toward surface positions with a lower concave curvature and, in turn, to the observed coarsening of the porous network. In order to distinguish between the extent of Pt dissolution/redeposition compared to surface mobility of Pt adatoms for the porosity reorganization, a potential-resolved analysis of the Pt and Ni leaching during activation and a series of 10 "load cycles" at 0.05 V s^{-1} (Figure 5) has been performed (see SI for details[22,62,70]). Consistent with our previous observations, activation is inevitably associated with a massive Ni dealloying and only minor Pt dissolution, which is close to the detection limit and at least 3 orders of magnitude lower

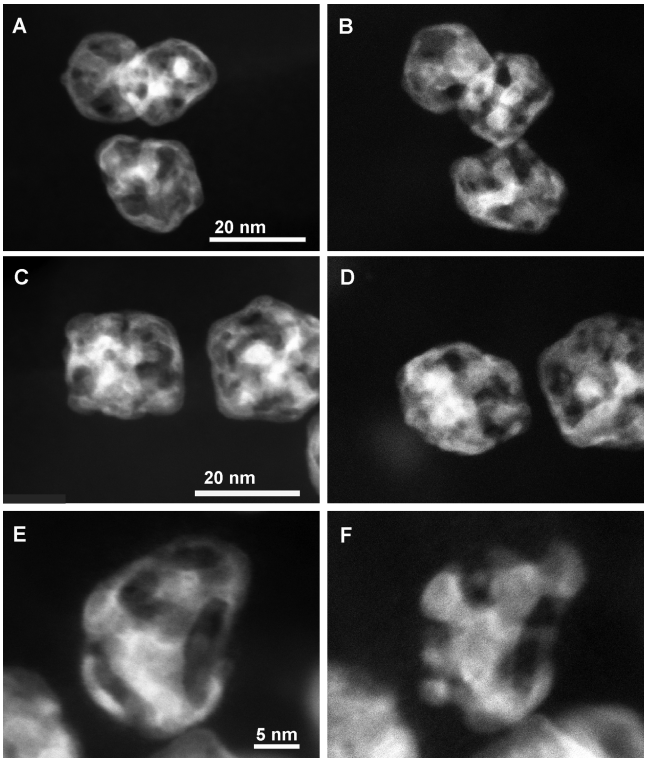

Figure 4. HAADF micrographs of selected, representative locations before (left column) and after (right column) 5000 degradation cycles between 0.4 and 1.0 V_{RHE} at 1.0 V s^{-1}.

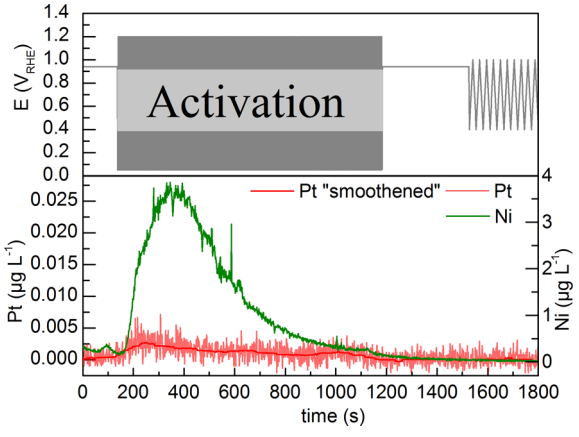

Figure 5. Online Ni and Pt leaching profile throughout the activation procedure, consisting of 200 cycles between 0.05 and 1.2 V_{RHE} with 0.5 V s^{-1}, and 10 cycles between 0.4 and 1.0 V_{RHE} with 0.05 V s^{-1}. To facilitate the interpretation of the Pt dissolution profile, both real and smoothened signal are provided.

DOI: 10.1021/acscatal.5b01151
ACS Catal. 2015, 5, 5000−5007

than Ni dissolution. Once the nanoparticles are fully activated, cycling up to 1.0 V_{RHE} does not trigger any significant dissolution above the detection limit. This result indicates that (i) the Ni is completely dissolved from the exposed surface under these conditions; (ii) the Ni rich core of the ligaments is protected by a Pt surface shell, preventing further major dealloying and suggesting that Ni surface segregation plays, at best, only a minor role in the porosity evolution; and (iii) the potential excursions related to the "load cycles" do not trigger detectable Pt dissolution after activation, confirming that Pt adatom diffusion is indeed the main driving force for the observed porosity coarsening. This degradation pathway is characteristic of the open network configuration.

To some extent it can be considered similar to agglomeration, as it is driven by surface energy minimization and does not require high potentials. However, although particle migration can be mitigated by tuning the particle size and/or catalyst loading,[61] the reorganization of the percolated network is inherent of the metastable nature of a nanoporous structure, which will be hard to circumvent even at potentials equivalent to the double layer region.[67] Note that in the case of conventional nanoparticle dispersion, such a process has a more limited impact, due to the lower surface energy of the typically more compact and thermodynamically stable configuration of nonporous structures, and due to the overlap with other ordinary degradation processes. Nevertheless, although our investigation is limited to percolated nanostructures, a similar process could be easily transferred to other nanoengineered open structures, as adatom diffusion would be inevitably detrimental to other kinds of high energy surfaces, like hollow configurations or nanoframes.

In order to simulate the potential excursions affecting the catalyst in the critical start-up and shut-down procedures, during which the potential can reach values up to 1.4 V_{RHE},[71] a second ADT procedure was applied. Because of the excursions to much more positive potentials, the extent of degradation is expected to be enhanced compared to the "load cycles". As shown in Figure 6, both ECSA and SA are indeed severely affected by 10 000 cycles under these potential conditions. While the active surface area (Figure 6A) appears to drastically drop throughout the whole degradation protocol to an overall loss of around 60%, the intrinsic activity decreases to 1.0 mA cm^{-2} and to 0.7 mA cm^{-2} after 5000 and 10 000 cycles (the SA values are taken at 0.9 V_{RHE}), respectively (Figure 6B). In contrast to the ADT with an upper potential limit of 1.0 V_{RHE}, continuous dealloying leads to a significant decrease in the Ni content of the catalyst even after activation (Figure 6B, inset). This is also confirmed by the potential-resolved dissolution profile of Pt and Ni during a series of 10 "start-up" cycles after activation (Figure 7). Notably, the oxidation/reduction process associated with cycling up to 1.4 V_{RHE} initiates detectable Pt dissolution, which leads to nickel dissolution from the bulk with an almost 3 times higher amount (Figure 7, inset), as similarly observed for the dissolution of Cu from a Pt−Cu material library.[22] The IL-TEM micrographs in Figure 8 before and after 5000 cycles confirm the extensive degradation reported by the electrochemical characterization on the nanoscale. Most strikingly, the catalyst structure appears to be severely affected by a complex combination of several degradation pathways. To separate the different routes, a large number of locations have been investigated, and the most representative ones are gathered in Figure 8 and S8. A common trait observed for several locations throughout the sample is porosity coarsening,

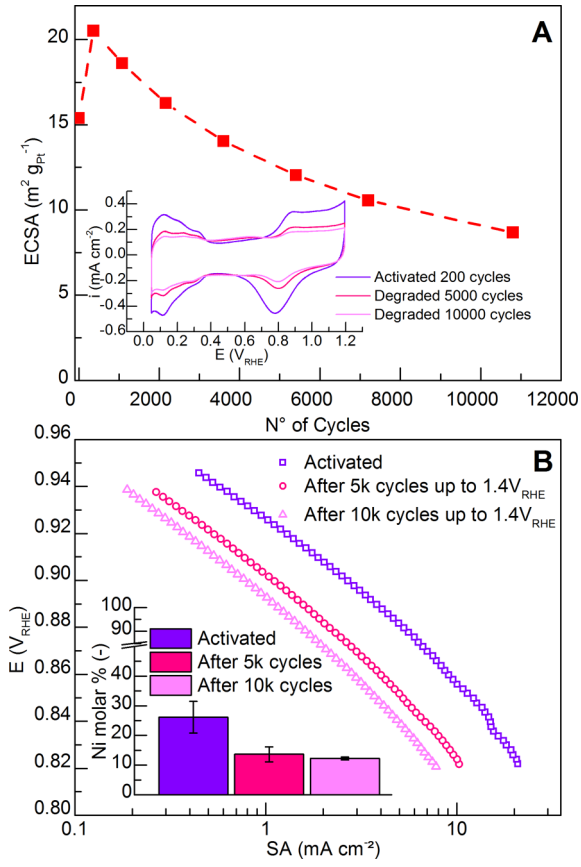

Figure 6. (A) ECSA vs degradation cycles, performed between 0.4 and 1.4 V_{RHE} at room temperature with 1.0 V s^{-1} scan rate, and representative CVs at defined intervals of the durability test (inset). (B) Tafel plots and Ni molar ratio evolution (inset) of the catalyst under study at the beginning of degradation, as well as after 5000 and 10 000 cycles of ADT; the kinetic data are obtained by normalizing the currents by the active surface area measured after each degradation interval.

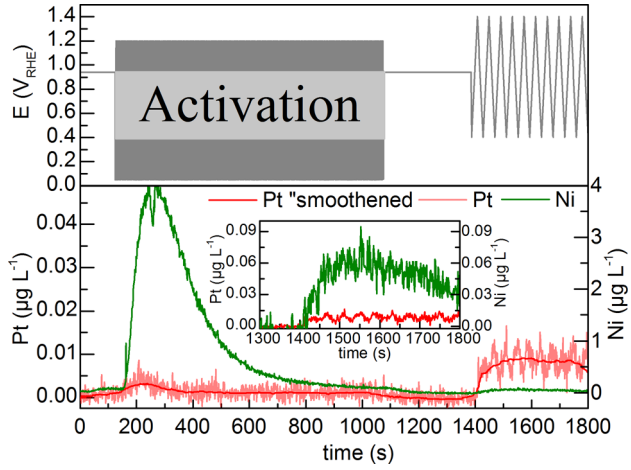

Figure 7. Online Ni and Pt dissolution profile throughout the activation procedure, consisting of 200 cycles between 0.05 and 1.2 V_{RHE} with 0.5 V s^{-1}, and during 10 cycles between 0.4 and 1.4 V_{RHE} with 0.05 V s^{-1}. To facilitate the interpretation of the Pt dissolution profile, both real and smoothened signal are provided. The inset includes a magnification of the dissolution profile during the last 10 cycles up to 1.4 V_{RHE}, which compares the dissolution amounts of both elements on the same scale.

DOI: 10.1021/acscatal.5b01151
ACS Catal. 2015, 5, 5000−5007

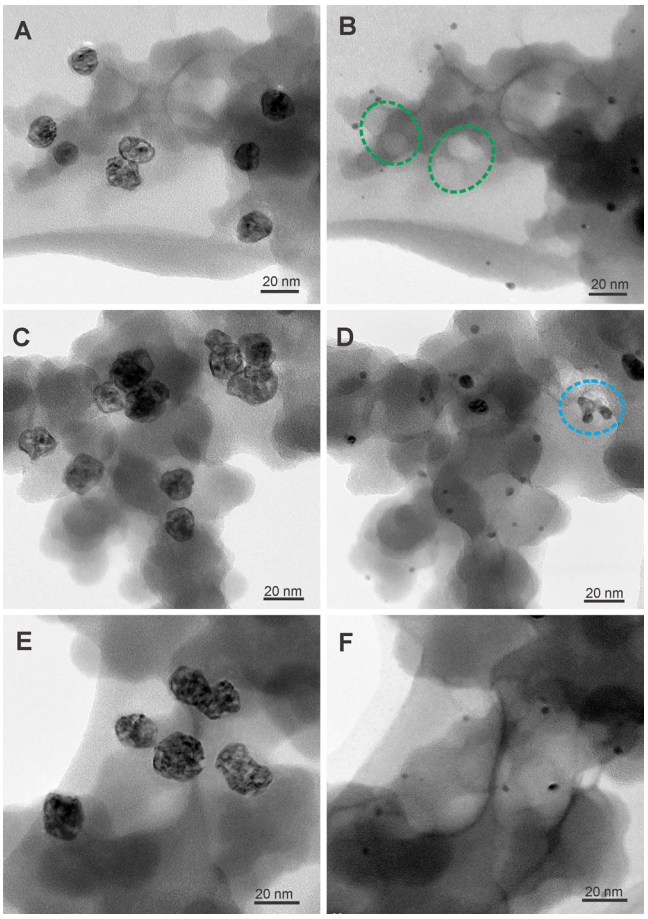

Figure 8. HR-TEM micrographs of selected locations before (left column) and after (right column) 5000 degradation cycles between 0.4 and 1.4 V_{RHE} at 1.0 V s^{-1}. The blue circles indicate a representative case of agglomeration of several particles, while the green ones represent areas of localized carbon corrosion eventually followed by particle detachment.

which combined with dealloying remains the important initial degradation mechanism. In contrast to the load cycles before, however, this does not result in a porous structure. After the "start-up" ADT cycles, the porosity appears completely disintegrated, and predominantly compact-sized nanoparticles of much smaller dimensions remain on the carbon support (Figure 8 and S8). This drastic change in catalyst morphology is quite evident in Figure S8 and the particle size distribution (PSD) therein: the size decreases from ca. 25 nm for the activated nanoporous particles toward a PSD centered about 5 nm after 5000 cycles (Figure S9). The porous structure at the high potentials reached in the "start-up" cycles is degrading much more rapidly, as significant Pt dissolution occurs. This process causes not only enhanced dealloying but also additional degradation by a solution phase Ostwald ripening process, leading to the formation of compact Wulff polyhedra. Note that these particles can then degrade further by different pathways. Actually, in a small number of locations, the so-produced compact nanoparticles undergo agglomeration, especially when they are in close proximity (Figure 8b, blue circle). By overlapping the before and after micrographs at different locations of the same sample, it appears that several particles have completely vanished. Interestingly, in many cases, the missing particles appear to leave behind a sort of imprint (Figure 8f, green circles), possibly related to some localized support corrosion catalyzed by the Pt nanoparticles.[72,73] Considering the large potential excursions and the growing quinone-hydroquinone peak visible at around 0.6 V_{RHE} in Figure6A (inset), this process is not unexpected. However, as the carbon structure in general shows only minor signs of deterioration (Figure 8d–f and S8), these particular ADTs at room temperature seem to reduce the impact of carbon oxidation to the metal–support interface. Thus, although it cannot be refuted that these imprints already existed before degradation and the particles have simply dissolved, it seems reasonable that a certain fraction of large particles detached from the surface after localized corrosion of the support. In summary, porosity loss and dealloying remain the predominant degradation routes in the case of a "start-up" regime for alloy particles in the size ranges considered here. However, in contrast to the load cycle potential region above, the overall process is exacerbated by the dissolution of Pt triggered by the excursions to more positive potentials, leading to a rapid porosity loss and the considerable decrease in mean particle size. Moreover, also localized corrosion of the support has been detected, which causes particle detachment and therefore adds to the extensive decay in ECSA, SA and MA.

CONCLUSIONS

We have herein reported a detailed analysis of the durability of a representative porous nanoparticulate system. The catalyst stability was investigated by two different ADTs intended to mirror the potential regimes expected during the nominal operative conditions of a fuel cell and the critical start-up and shut-down events. Although porous nanoparticles are an interesting class of highly active catalysts for oxygen reduction, the long-term stability of the porosity on the nanoparticle scale and in fuel cell relevant operative conditions has to be assessed critically. Potential excursions inevitably trigger reorganization of the percolated network toward the minimization of the nanoscale curvature. The extent of the degradation process is strongly related to the potential window (i.e., the intensity of the excursions). Even under the relatively mild "load cycles" porosity coarsening yields a loss in mass activity of around 40% within the experimental time frame. The more positive potentials associated with the start-up cycles clearly accelerate the process due to the initiation of several additional degradation processes, leading to the complete disintegration of the beneficial porous configuration and a severe deterioration of the electrochemical performance. These results highlight some important shortcomings in terms of durability of this catalytic system, which need to be addressed prior to any future industrial application. Albeit limited to the investigation of particular porous nanostructures, this study demonstrates important aspects that could potentially affect any high surface energy configuration considered as catalyst for electrochemical energy conversion purposes.

ASSOCIATED CONTENT

Supporting Information

The Supporting Information is available free of charge on the ACS Publications website at DOI: 10.1021/acscatal.5b01151.

Description of the synthesis procedure, further details concerning the experimental techniques employed, and additional material about the study (PDF)

DOI: 10.1021/acscatal.5b01151
ACS Catal. 2015, 5, 5000–5007

AUTHOR INFORMATION

Corresponding Author

*E-mail: c.baldizzone@mpie.de. Phone: +49 211 6792 898.

Present Address

[#]National Institute of Chemistry, Hajdrihova 19, 1000 Ljubljana, Slovenia.

Notes

The authors declare no competing financial interest.

ACKNOWLEDGMENTS

We thank Andrea Mingers for the ICP-MS measurements and assistance with data elaboration. C.B. acknowledges the IMPRS-SurMat for funding. P.S and L.G. acknowledge financial support by the German Research Foundation (DFG). M.H. gratefully acknowledges financial support by the German Research Foundation (DFG) through grant HE 7192/1-1. This research was supported by a Marie Curie Intra European Fellowship within the 7th European Community Framework Programme (acknowledged by N.H.).

REFERENCES

(1) Debe, M. K. *Nature* **2012**, *486*, 43−51.
(2) Erlebacher, J.; Aziz, M. J.; Karma, A.; Dimitrov, N.; Sieradzki, K. *Nature* **2001**, *410*, 450−453.
(3) Ding, Y.; Chen, M. *MRS Bull.* **2009**, *34*, 569−576.
(4) Attard, G. S.; Bartlett, P. N.; Coleman, N. R. B.; Elliott, J. M.; et al. *Science* **1997**, *278*, 838−840.
(5) Liang, H.-P.; Zhang, H.-M.; Hu, J.-S.; Guo, Y.-G.; Wan, L.-J.; Bai, C.-L. *Angew. Chem., Int. Ed.* **2004**, *43*, 1540−1543.
(6) Yang, R. Y.; Leisch, J.; Strasser, P.; Toney, M. F. *Chem. Mater.* **2010**, *22*, 4712−4720.
(7) Yang, D.; Sun, S.; Meng, H.; Dodelet, J.-P.; Sacher, E. *Chem. Mater.* **2008**, *20*, 4677−4681.
(8) Pasricha, R.; Bala, T.; Biradar, A. V.; Umbarkar, S.; Sastry, M. *Small* **2009**, *5*, 1467−1473.
(9) Peng, Z.; Yang, H. *J. Am. Chem. Soc.* **2009**, *131*, 7542−7543.
(10) Kibsgaard, J.; Gorlin, Y.; Chen, Z.; Jaramillo, T. F. *J. Am. Chem. Soc.* **2012**, *134*, 7758−7765.
(11) Strasser, P.; Koh, S.; Greeley, J. *Phys. Chem. Chem. Phys.* **2008**, *10*, 3670−3683.
(12) Srivastava, R.; Mani, P.; Hahn, N.; Strasser, P. *Angew. Chem., Int. Ed.* **2007**, *46*, 8988−8991.
(13) Koh, S.; Strasser, P. *J. Am. Chem. Soc.* **2007**, *129*, 12624−12625.
(14) Wang, R.; Xu, C.; Bi, X.; Ding, Y. *Energy Environ. Sci.* **2012**, *5*, 5281−5286.
(15) Liu, L.; Pippel, E.; Scholz, R.; Gösele, U. *Nano Lett.* **2009**, *9*, 4352−4358.
(16) Snyder, J.; Livi, K.; Erlebacher, J. *Adv. Funct. Mater.* **2013**, *23*, 5494−5501.
(17) Wang, D.; Zhao, P.; Li, Y. *Sci. Rep.* **2011**, *1*, 37.
(18) Snyder, J.; McCue, I.; Livi, K.; Erlebacher, J. *J. Am. Chem. Soc.* **2012**, *134*, 8633−8645.
(19) Snyder, J.; Asanithi, P.; Dalton, A. B.; Erlebacher, J. *Adv. Mater.* **2008**, *20*, 4883−4886.
(20) Shui, J.-l.; Chen, C.; Li, J. C. M. *Adv. Funct. Mater.* **2011**, *21*, 3357−3362.
(21) Dursun, A.; Pugh, D. V.; Corcoran, S. G. *J. Electrochem. Soc.* **2005**, *152*, B65−B72.
(22) Schuppert, A. K.; Savan, A.; Ludwig, A.; Mayrhofer, K. J. J. *Electrochim. Acta* **2014**, *144*, 332−340.
(23) Oezaslan, M.; Heggen, M.; Strasser, P. *J. Am. Chem. Soc.* **2011**, *134*, 514−524.
(24) Gan, L.; Heggen, M.; Rudi, S.; Strasser, P. *Nano Lett.* **2012**, *12*, 5423−5430.
(25) McCue, I.; Snyder, J.; Li, X.; Chen, Q.; Sieradzki, K.; Erlebacher, J. *Phys. Rev. Lett.* **2012**, *108*, 225503−225505.
(26) Li, X.; Chen, Q.; McCue, I.; Snyder, J.; Crozier, P.; Erlebacher, J.; Sieradzki, K. *Nano Lett.* **2014**, *14*, 2569−2577.
(27) Jeyabharathi, C.; Hodnik, N.; Baldizzone, C.; Meier, J. C.; Heggen, M.; Phani, K. L. N.; Bele, M.; Zorko, M.; Hocevar, S.; Mayrhofer, K. J. J. *ChemCatChem* **2013**, *5*, 2627−2635.
(28) Oezaslan, M.; Hasché, F.; Strasser, P. *J. Phys. Chem. Lett.* **2013**, *4*, 3273−3291.
(29) Chen, H. M.; Liu, R.-S.; Lo, M.-Y.; Chang, S.-C.; Tsai, L.-D.; Peng, Y.-M.; Lee, J.-F. *J. Phys. Chem. C* **2008**, *112*, 7522−7526.
(30) Strasser, P.; Koh, S.; Anniyev, T.; Greeley, J.; More, K.; Yu, C.; Liu, Z.; Kaya, S.; Nordlund, D.; Ogasawara, H.; Toney, M. F.; Nilsson, A. *Nat. Chem.* **2010**, *2*, 454−460.
(31) Bae, J. H.; Han, J.-H.; Chung, T. D. *Phys. Chem. Chem. Phys.* **2012**, *14*, 448−463.
(32) Birkin, P. R.; Elliott, J. M.; Watson, Y. E. *Chem. Commun.* **2000**, 1693−1694.
(33) Han, J.-H.; Lee, E.; Park, S.; Chang, R.; Chung, T. D. *J. Phys. Chem. C* **2010**, *114*, 9546−9553.
(34) Mahmoud, M. A.; Saira, F.; El-Sayed, M. A. *Nano Lett.* **2010**, *10*, 3764−3769.
(35) Stamenkovic, V. R.; Fowler, B.; Mun, B. S.; Wang, G.; Ross, P. N.; Lucas, C. A.; Marković, N. M. *Science* **2007**, *315*, 493−497.
(36) Martínez de la Hoz, J. M.; Balbuena, P. B. *J. Phys. Chem. C* **2011**, *115*, 21324−21333.
(37) Nesselberger, M.; Roefzaad, M.; Fayçal Hamou, R.; Ulrich Biedermann, P.; Schweinberger, F. F.; Kunz, S.; Schloegl, K.; Wiberg, G. K. H.; Ashton, S.; Heiz, U.; Mayrhofer, K. J. J.; Arenz, M. *Nat. Mater.* **2013**, *12*, 919−924.
(38) López-Cudero, A.; Solla-Gullón, J.; Herrero, E.; Aldaz, A.; Feliu, J. M. *J. Electroanal. Chem.* **2010**, *644*, 117−126.
(39) Kucernak, A.; Jiang, J. *Chem. Eng. J.* **2003**, *93*, 81−90.
(40) Wu, Y.; Wang, D.; Niu, Z.; Chen, P.; Zhou, G.; Li, Y. *Angew. Chem., Int. Ed.* **2012**, *51*, 12524−12528.
(41) Chen, C.; Kang, Y.; Huo, Z.; Zhu, Z.; Huang, W.; Xin, H. L.; Snyder, J. D.; Li, D.; Herron, J. A.; Mavrikakis, M.; Chi, M.; More, K. L.; Li, Y.; Markovic, N. M.; Somorjai, G. A.; Yang, P.; Stamenkovic, V. R. *Science* **2014**, *343*, 1339−1343.
(42) Hodnik, N.; Zorko, M.; Bele, M.; Hočevar, S.; Gaberšček, M. *J. Phys. Chem. C* **2012**, *116*, 21326−21333.
(43) Chen, S.; Gasteiger, H. A.; Hayakawa, K.; Tada, T.; Shao-Horn, Y. *J. Electrochem. Soc.* **2010**, *157*, A82−A97.
(44) Ding, Y.; Kim, Y. J.; Erlebacher, J. *Adv. Mater.* **2004**, *16*, 1897−1900.
(45) Chang, S. L. Y.; Barnard, A. S.; Dwyer, C.; Hansen, T. W.; Wagner, J. B.; Dunin-Borkowski, R. E.; Weyland, M.; Konishi, H.; Xu, H. *J. Phys. Chem. Lett.* **2012**, *3*, 1106−1110.
(46) Cui, C.; Ahmadi, M.; Behafarid, F.; Gan, L.; Neumann, M.; Heggen, M.; Cuenya, B. R.; Strasser, P. *Faraday Discuss.* **2013**, *162*, 91−112.
(47) Gan, L.; Heggen, M.; O'Malley, R.; Theobald, B.; Strasser, P. *Nano Lett.* **2013**, *13*, 1131−1138.
(48) Cui, C. H.; Gan, L.; Neumann, M.; Heggen, M.; Cuenya, B. R.; Strasser, P. *J. Am. Chem. Soc.* **2014**, *136*, 4813−4816.
(49) Gan, L.; Cui, C. H.; Rudi, S.; Strasser, P. *Top. Catal.* **2014**, *57*, 236−244.
(50) Galeano, C.; Meier, J. C.; Peinecke, V.; Bongard, H.; Katsounaros, I.; Topalov, A. A.; Lu, A.; Mayrhofer, K. J. J.; Schüth, F. *J. Am. Chem. Soc.* **2012**, *134*, 20457−20465.
(51) Rudi, S.; Gan, L.; Cui, C.; Gliech, M.; Strasser, P. *J. Electrochem. Soc.* **2015**, *162*, F403−F409.
(52) Cui, C.; Gan, L.; Li, H.-H.; Yu, S.-H.; Heggen, M.; Strasser, P. *Nano Lett.* **2012**, *12*, 5885−5889.
(53) Meier, J. C.; Galeano, C.; Katsounaros, I.; Topalov, A. A.; Kostka, A.; Schüth, F.; Mayrhofer, K. J. J. *ACS Catal.* **2012**, *2*, 832−843.
(54) Mayrhofer, K. J. J.; Ashton, S. J.; Meier, J. C.; Wiberg, G. K. H.; Hanzlik, M.; Arenz, M. *J. Power Sources* **2008**, *185*, 734−739.

DOI: 10.1021/acscatal.5b01151
ACS Catal. 2015, 5, 5000−5007

(55) Baldizzone, C.; Mezzavilla, S.; Carvalho, H. W. P.; Meier, J. C.; Schuppert, A. K.; Heggen, M.; Galeano, C.; Grunwaldt, J.-D.; Schüth, F.; Mayrhofer, K. J. J. *Angew. Chem., Int. Ed.* **2014**, *53*, 14250−14254.
(56) Liu, Z.; Xin, H.; Yu, Z.; Zhu, Y.; Zhang, J.; Mundy, J. A.; Muller, D. A.; Wagner, F. T. *J. Electrochem. Soc.* **2012**, *159*, F554−F559.
(57) Gan, L.; Cui, C.; Heggen, M.; Dionigi, F.; Rudi, S.; Strasser, P. *Science* **2014**, *346*, 1502−1506.
(58) Yu, Y.; Xin, H. L.; Hovden, R.; Wang, D.; Rus, E. D.; Mundy, J. A.; Muller, D. A.; Abruña, H. D. *Nano Lett.* **2011**, *12*, 4417−4423.
(59) Hasché, F.; Oezaslan, M.; Strasser, P. *ChemCatChem* **2011**, *3*, 1805−1813.
(60) Xin, H. L.; Mundy, J. A.; Liu, Z.; Cabezas, R.; Hovden, R.; Kourkoutis, L. F.; Zhang, J.; Subramanian, N. P.; Makharia, R.; Wagner, F. T.; Muller, D. A. *Nano Lett.* **2011**, *12*, 490−497.
(61) Meier, J. C.; Galeano, C.; Katsounaros, I.; Witte, J.; Bongard, H. J.; Topalov, A. A.; Baldizzone, C.; Mezzavilla, S.; Schüth, F.; Mayrhofer, K. J. J. *Beilstein J. Nanotechnol.* **2014**, *5*, 44−67.
(62) Topalov, A. A.; Katsounaros, I.; Auinger, M.; Cherevko, S.; Meier, J. C.; Klemm, S. O.; Mayrhofer, K. J. J. *Angew. Chem., Int. Ed.* **2012**, *51*, 12613−12615.
(63) Jovanovič, P.; Pavlišič, A.; Šelih, V. S.; Šala, M.; Hodnik, N.; Bele, M.; Hočevar, S.; Gaberšček, M. *ChemCatChem* **2014**, *6*, 449−453.
(64) Erlebacher, J.; McCue, I. *Acta Mater.* **2012**, *60*, 6164−6174.
(65) Xu, Q. M.; He, T.; Wipf, D. *Langmuir* **2007**, *23*, 9098−9103.
(66) Xu, Q.; Kreidler, E.; Wipf, D. O.; He, T. *J. Electrochem. Soc.* **2008**, *155*, B228−B231.
(67) Xu, Q.; Kreidler, E.; He, T. *Electrochim. Acta* **2010**, *55*, 7551−7557.
(68) Jubrias, J. J. M.; Hidalgo, M.; Marcos, M. L.; Velasco, J. G. *Surf. Sci.* **1996**, *366*, 239−250.
(69) Tian, N.; Zhou, Z. Y.; Sun, S. G.; Ding, Y.; Wang, Z. L. *Science* **2007**, *316*, 732−735.
(70) Schuppert, A. K.; Topalov, A. A.; Katsounaros, I.; Klemm, S. O.; Mayrhofer, K. J. J. *J. Electrochem. Soc.* **2012**, *159*, F670−F675.
(71) Gu, W.; Carter, R. N.; Yu, P. T.; Gasteiger, H. A. *ECS Trans.* **2007**, *11*, 963−973.
(72) Roen, L. M.; Paik, C. H.; Jarvi, T. D. *Electrochem. Solid-State Lett.* **2004**, *7*, A19−A22.
(73) Dam, V. A. T.; Jayasayee, K.; de Bruijn, F. A. *Fuel Cells* **2009**, *9*, 453−462.

DOI: 10.1021/acscatal.5b01151
ACS Catal. 2015, 5, 5000−5007